Noise Radiation from a Leading-Edge Slat

David P. Lockard* and Meelan M. Choudhari†
NASA Langley Research Center, Hampton, VA 23681

This paper extends our previous computations of unsteady flow within the slat cove region of a multi-element high-lift airfoil configuration, which showed that both statistical and structural aspects of the experimentally observed unsteady flow behavior can be captured via 3D simulations over a computational domain of narrow spanwise extent. Although such narrow domain simulation can account for the spanwise decorrelation of the slat cove fluctuations, the resulting database cannot be applied towards acoustic predictions of the slat without invoking additional approximations to synthesize the fluctuation field over the rest of the span. This deficiency is partially alleviated in the present work by increasing the spanwise extent of the computational domain from 37.3% of the slat chord to nearly 226% (i.e., 15% of the model span). The simulation database is used to verify consistency with previous computational results and, then, to develop predictions of the far-field noise radiation in conjunction with a frequency-domain Ffowcs-Williams Hawkings solver.

Nomenclature

a	speed of sound
c	stowed chord
c_s	slat chord
M	Mach number
p	pressure
u, v, w	Cartesian fluid velocity components
U, V, W	time-averaged velocity components
x, y, z	Cartesian coordinates

Greek:

ρ	fluid density
θ	azimuthal angle ($x-y$ plane)
ϕ	polar angle ($z-y$ plane)

Superscript:

$'$	perturbation quantity (e.g. $\rho' = \rho - \rho_\infty$)

Subscript:

∞	freestream quantity

I. Introduction

The non-propulsive (or airframe) sources of aircraft noise include high-lift devices (i.e., leading-edge slat and trailing-edge flaps) and the aircraft undercarriage. The ranking of these sources is configuration dependent; however, both model scale tests[1–6] and flyover noise measurements[7] have identified the leading-edge slat as a prominent source of airframe noise during aircraft approach. The slat noise spectrum is typically broadband, but may include one or more narrower peaks associated with aerodynamic and/or aeroacoustic resonances. Previous measurements indicate that the broadband spectrum has a maximum near $St \sim$ 1-3 (where the Strouhal number $St = fc_s/U_\infty$ is based on the free-stream velocity U_∞ and slat chord c_s), and exhibits peak directivity in the lower aft quadrant at the corresponding frequency.[8] The overall sound pressure level (OASPL) for slat noise sources has been noted to scale with $M^{4.5}$ by Dobrzynksi[8] and M^5 by Guo,[9,10] where M denotes the free-stream/flight Mach number. Mendoza[6] found that the OASPL scaled with M^5, but with $M^{4.x}$ in the range of mid to high frequencies. However, as discussed in references 8 and 10, the physical mechanisms underlying the observed characteristics of slat noise have not been fully explained as yet.

An essential ingredient to developing physics based predictions of airframe noise involves synergistic combinations of experiments and numerical simulations for unit configurations. Recent studies of this type have provided a number of useful physical insights into the noise source mechanisms that are responsible for the dominant features of the measured slat- and flap-noise spectra. Specifically, the high-frequency spectral hump in the slat noise measurements at NASA[2,5] has been attributed to vortex shedding from a finite thickness slat trailing edge,[11,12] whereas the broadband component of slat noise at lower frequencies has been linked with the interaction between unsteady vorticity structures in the slat cove region and the adjacent features of the high-lift geometry (viz., the slat trailing edge and the gap region between the slat and the main element).[13–15] The 2-D computations of this type helped clarify the cause-effect relationships between the near-field flow structures and the far-field noise; however, a further assessment of these computations[16] indicated excessively energetic vorticity structures in comparison with the PIV measurements.[17] 3-D computations over a narrow

*Aerospace Technologist, Computational AeroSciences Branch, Mail Stop 128, Senior Member, AIAA
†Aerospace Technologist, Computational AeroSciences Branch, Mail Stop 128, Associate Fellow, AIAA

portion of the model span[20] led to significant improvement in that regard, yielding a favorable comparison with the PIV measurements.[17] The importance of 3-D fluctuations in determining the unsteady dynamics within the cove region has also been confirmed via computations for other high-lift configurations and using alternative numerical algorithms.[18,19] However, acoustic predictions based on nearfield simulations of this type are still missing, partly because of the narrow spanwise extent of the computational domain (i.e., acoustically compact within the dominant range of the nearfield acoustic spectrum).

The acoustic sources in the slat cove have been investigated experimentally[17] using the 30P/30N model. The 30P/30N model tested in the Basic Aerodynamic Research Tunnel (BART) at NASA Langley Research Center represents a generic, three-element, zero-sweep high-lift configuration with slat and flap deflections of 30 degrees each. The slat chord and flap chord of the model are equal to 15% and 30%, respectively, of the stowed chord of 18 in (0.457 m). For the approach configuration, the slat gap is 2.95%; the flap gap is 1.27%; and the slat and flap overhang settings are equal to -2.95% and 0.25%, respectively. Reference 21 provides a definition of these rigging parameters. At the test Mach number of M = 0.17, the Reynolds number Re_c based on the stowed chord of the BART model, corresponds to 1.7 million. While this Reynolds number is substantially lower in comparison with full-scale applications, the BART experiment is still suitable for validating numerical predictions of the slat cove noise sources as described in Reference 20. The BART measurements[17] consist of steady surface pressure measurements, plus extensive two-dimensional (2D) particle image velocimetry (PIV) data within the mid-span plane of the model.

To help enable physics based predictions of the slat cove noise, the present paper extends the earlier computations by increasing the spanwise extent of the computational domain in reference[20] from 1" (37.3% of the slat chord) to 6" (226% of the slat chord or 15% of the model span) while maintaining the same spanwise resolution. The simulation database is used to verify consistency with the results of the previous computation and, then, to develop predictions of the far-field noise radiation in conjunction with a frequency-domain Ffowcs-Williams Hawkings solver. A brief description of the computational model and methodology is given below, followed by illustrative results for both the nearfield unsteadiness within the slat cove and the radiated acoustic field away from the slat.

II. Computational Simulations

The computational procedure closely parallels that used during the narrow-spanwise-domain simulations in Ref. 20, in order to isolate the effects of spanwise domain length as much as possible. Version 6 of the CFL3D[22] flow solver developed at NASA Langley Research Center is used to solve the 3-D, time-dependent, Reynolds-averaged Navier-Stokes (RANS) equations using a finite-volume formulation; the viscous fluxes in all three grid coordinates were retained during the present simulations. The simulation uses the third-order upwind scheme with flux-difference splitting, which has been shown to provide second order spatial accuracy in previous applications of CFL3D.

II.A. Configurations and Grids

The 30P30N[21] high-lift system was simulated in free air without any of the wind-tunnel walls. The trailing edges of all three elements have a finite thickness. However, for computational purposes, all of the trailing edges (including the cusp or first edge of the slat) were artificially sharpened while preserving the camber of the respective sections. Based on previous studies,[11,12] sharpening the trailing-edge should only affect vortex shedding caused by trailing-edge bluntness and not the cove dynamics. Sharpening the first edge on the slat has little effect on the cove shear layer because the cusp is merely serving as a fixed separation point like the corner of a backward facing step. As the focus of the current study is the broadband noise source associated with the slat shear layer, removing points around the edges allowed additional grid points to resolve the slat cove dynamics and nearfield acoustic radiation. The investigated configuration corresponds to 4-degrees angle of attack in BART,[17] which approximates the mean slat loading for a free-flight configuration at 5.5 degrees of attack. Considerable effort was spent in grid generation to allow adequate resolution of the relevant aerodynamic and acoustic phenomena in an efficient manner. The block structured, $x-y$ planar grid shown in figure 1 contained a total of 563,741 points in 77 blocks. Care was taken so that the first point off the solid surfaces was at $y^+ \sim O(1)$. To generate the 3-D grids, the planar mesh was replicated along the span over a distance of 2.24 slat chords using 385 points for a total grid point count of 186 million. Patched interfaces were employed but restricted to regions away from the slat.

Characteristic boundary conditions were used along the far-field boundaries in the $x-y$ plane, except for extrapolation from the interior at the downstream boundary. Periodic boundary conditions were used across the spanwise boundaries of the computational domain. No attempt was made to resolve the end effects present in the experiments. No-slip conditions were imposed at the solid surfaces, along with an adiabatic wall thermal boundary condition.

The two-equation Shear Stress Transport (SST) model of Menter[25] is used to capture the mean flow behavior chosen to capture the effects of the unresolved scales of motion in regions away from the slat cove region, whereas the turbulence

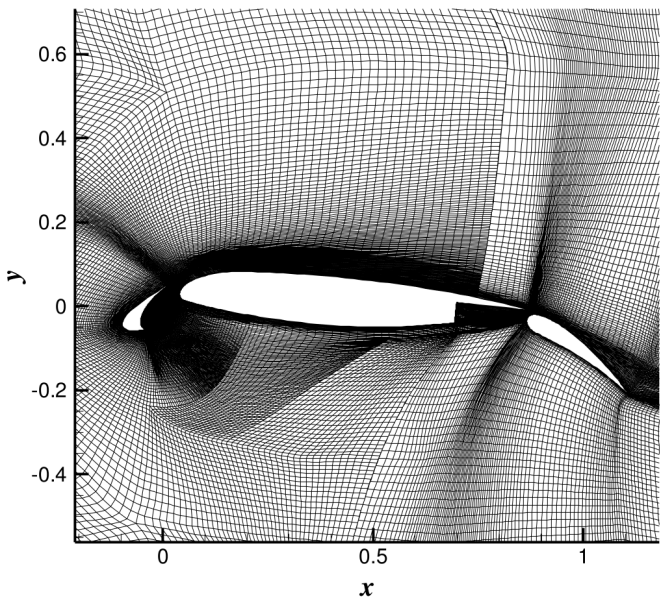

Figure 1. Planar view of grid (every other point).

production term in the turbulence transport equations was switched off within the cove region[20] to eliminate the excessive diffusive effects of the turbulence model on the resolved unsteady flow structures. Due to a lack of transition data along the solid surfaces (as well as to maintain consistency with the previous 2D simulations,[14–16] the flow within the RANS regions was treated as fully turbulent, allowing the boundary layer transition locations along all three elements to be determined by the SST turbulence model.

The code employs a dual time-stepping algorithm with subiterations used to converge the solution within each time step. We used 15 subiterations per time step. Two simulations have been performed with constant non-dimensional time steps of $dt\ a_\infty/c = 0.0016464$ and 0.0008232 or $dt\ U_\infty/c = 0.00968$ and 0.004842. The corresponding convective scales for the flow to traverse the stowed chord of the airfoil are 3573 and 7146 time steps, respectively. The time step used in the current simulations is larger than those used in previous simulations of the 30P30N configuration[16,20] because the trailing-edges have been sharpened to avoid having to resolve the small trailing-edge thickness that would have enabled the simulations to capture any high-frequency vortex shedding behind the edges. While the decision to sharpen the edges thereby enabling the use of a larger time step was made purely for reasons of computational expediency, a posteriori analysis[15] suggests that there is no major coupling between the broadband noise associated with the slat cove and the narrow band source associated with vortex shedding behind the slat trailing edge.

The simulation procedure includes several steps. First, a steady-state computation was used to set up the basic mean flow, followed by an unsteady calculation with random suction and blowing applied to different spanwise and azimuthal sections of the slat in order to accelerate the onset of 3D, unsteady flow structures. The forcing did not exceed 3% of the freestream velocity. The forcing was turned off after significant unsteadiness was observed, typically a few hundred time steps into the unsteady calculation. The simulation was then run for 20,000 time steps to allow the transient flowfield to wash out before collecting time records. During the transient phase, well-resolved, unsteady structures develop in the slat cove region. Furthermore, there is some unsteadiness associated with a separated region on the flap. The grid is too coarse to resolve the unsteady flow around the flap, and these fluctuations eventually settle down to levels that do not significantly impact the slat cove region. In the real flow, the oscillations in the flap separated region are probably persistent and much stronger, but the purpose of the current study is to isolate the slat cove dynamics. Therefore, the observed damping behavior in the flap region is actually intended and advantageous. Averaged flow quantities were produced by time-averaging over 30,000 time steps for the larger dt, and 52,000 time steps for the smaller dt. The number of averages was increased by spatially averaging over the span. Although shear layers can exhibit inhomogeneous spanwise behavior, over the relatively large length scales corresponding to the wavelength of the dominant acoustic frequencies, spanwise homogeneity of the flow statistics is a reasonable assumption.

III. Results

III.A. Mean Flow

The streamlines around the high-lift system are shown in the figure 2. The expected recirculation zone in the slat cove is seen in 2(a). In the global view in 2(b), a recirculation bubble can be seen on the flap. Unsteady excursions of the flap separation point caused the overall lift to change over a long time scale (multiple flow through times over the model). Although experimentally one can wait long enough for the flow to stabilize or take enough samples to average out the migration, running a CFD simulation long enough can be prohibitive. Even though we ran the code much longer than usual to wash out the initial transients, the lift still migrated during the computations. The lift coefficient decreased from approximately $C_L = 2.55$ to $C_L = 2.50$ during the large time-step calculation. The small time-step simulation had the benefit of restarting from the previous calculation and more of the transient had been washed out. During the small time-step calculation, the lift coefficient only varied between 2.50 and 2.52. Nonetheless, the lift fluctuations caused by the slat cove dynamics is only around ± 0.005 and much smaller than that caused by the movement of the flap separation point. However, the slat cove fluctuations occur at much higher frequencies that can be isolated from the slow variations associated with the flap unsteadiness.

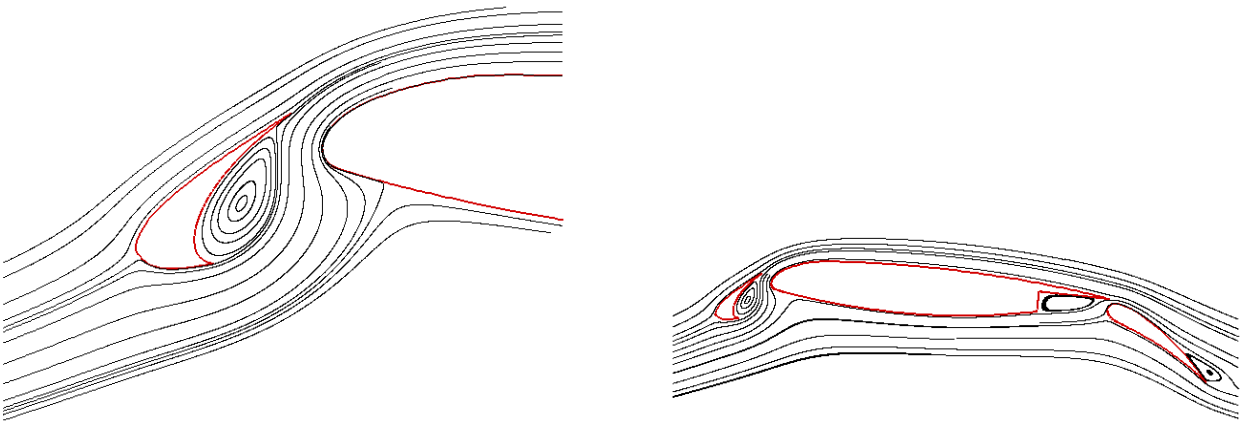

(a) (b)

Figure 2. Streamlines around the airfoil.

The coefficient of pressure on the high-lift system is presented in figure 3. The results from the calculations at the two time steps are included. The data was generated by averaging over time, then averaging over the span by assuming the flow is basically homogeneous in that direction. The slight jump on the pressure side at $x/c = 0.7$ is caused by the geometric discontinuity where the flap cove begins. Although the lift drifted during the large time step calculation, the influence on the surface pressure can not be seen on this scale. The drift has a larger influence on the calculation of the fluctuating pressure levels. To minimize the effect of the drift, the root-mean-square (rms) levels were calculated over each segment of a fixed time, 1000 time steps for the larger dt and 2000 time steps for the smaller dt. Over each of these segments, the perturbations were calculated relative to the short-time mean for the segment. A subsequent average was performed over rms levels from all of these segments. A comparison of the calculated Cp'_{rms} is shown in figure 4. Using this procedure, the results from the two calculations are quite similar, indicating that the slow variations in the flow field have a minimal influence on the fluctuations of interest. The peak around $x/c = 0.85$ is associated with a very localized region of unsteadiness at the trailing edge of the main element. Although the grid is relatively coarse in the flap cove, there is still some unsteadiness that develops and interacts with the edge. Although the spike at the edge is quite high, the area that sees high fluctuation levels is quite small, so the overall impact on the radiated noise is small. A close-up of the Cp'_{rms} field on the slat in figure 5 shows that the fluctuation levels are nearly identical between the two calculations. Although the smaller time step should enable higher frequencies to be resolved, the impact on the overall surface pressure fluctuation levels is minimal.

Although the spanwise direction is assumed to be periodic, the spanwise extent is sufficient to all the flow around the slat to exhibit considerable three-dimensional variation as can be seen in the instantaneous vorticity magnitude plot in figure 6(a). Although both calculations exhibit similar behavior, the results from the smaller dt were used to generate the figure. Spanwise rollers can be seen near the slat cusp that breakup into more random structures as they propagate along the shear layer. The shear layer rolls up into discrete spanwise vortices almost immediately downstream of the cusp. The quasi-2D vortices soon develop spanwise deformations that amplify with downstream distance, resulting in predominantly 3D vorticity structures in the downstream region. The 3D nature develops well upstream of the reattachment location. The plot of the spanwise vorticity, $\omega_z c/U_\infty$, in 6 (b) shows that some of the vortices recirculate within

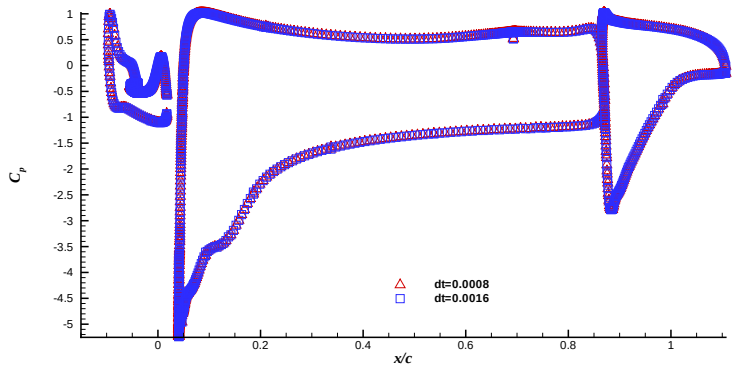

Figure 3. Coefficient of pressure on the airfoil.

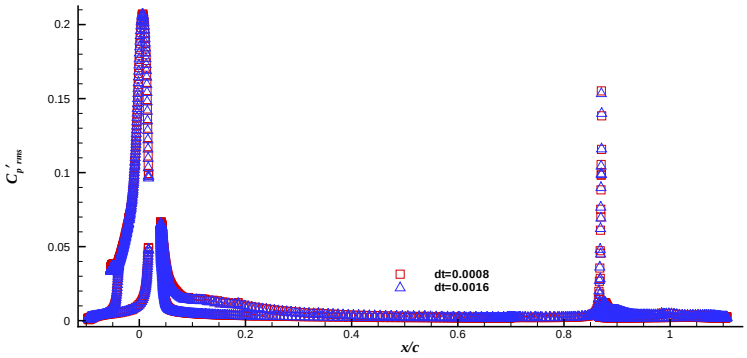

Figure 4. Fluctuating pressure on the airfoil.

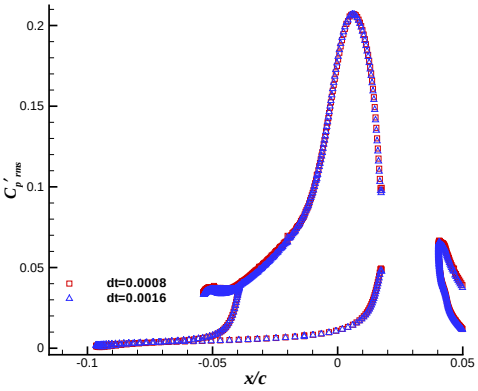

Figure 5. Fluctuating pressure on the slat.

the slat cove before eventually exiting through the slat gap. The rapid distortion of the structures near the reattachment point and the subsequent propagation past the slat trailing edge can be important sources of noise.

The averaged spanwise vorticity is presented in figure 7. On this scale, very little difference can be observed between the two simulations. However, the 2-D turbulent kinetic energy normalized by the free-stream velocity, $\frac{1}{2}(< u'u' > + < v'v' >)/U_\infty^2$, does reveal that the fluctuation levels in the smaller time step calculation are slightly higher in the shear layer near the cusp as show in figure 8. The computed behavior of both the mean vorticity distribution and TKE in the slat cove region is exactly analogous to the earlier results in reference 20 using a narrow spanwise domain. The current results do show slightly higher fluctuation levels near the reattachment point which is likely attributable to the beneficial effects of the finer resolution on resolving the vortices in the slat shear layer.

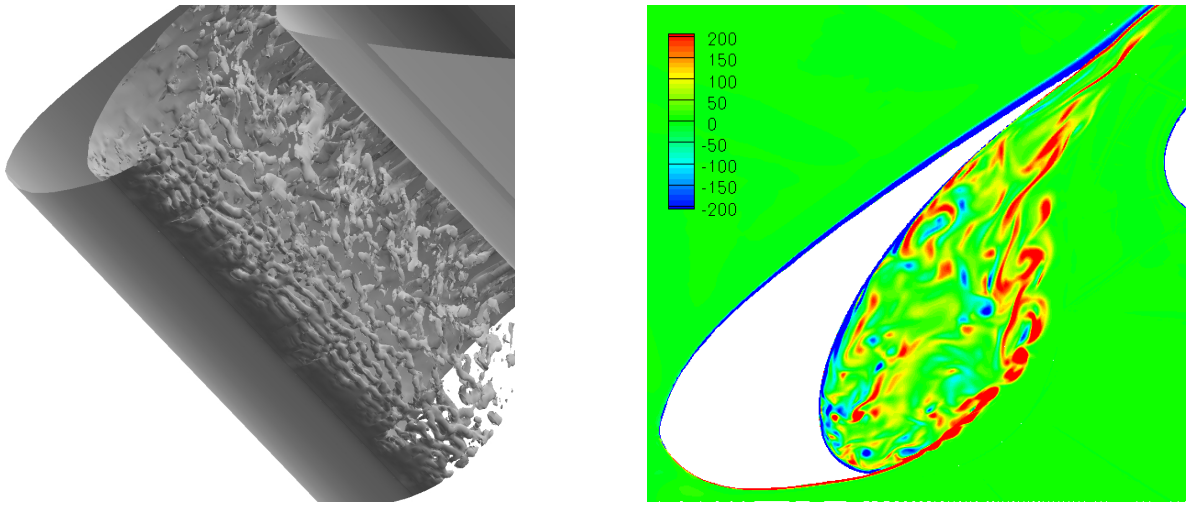

(a) Vorticity Magnitude (b) Spanwise vorticity, $\omega_z c/U_\infty$

Figure 6. Instantaneous vorticity around the slat.

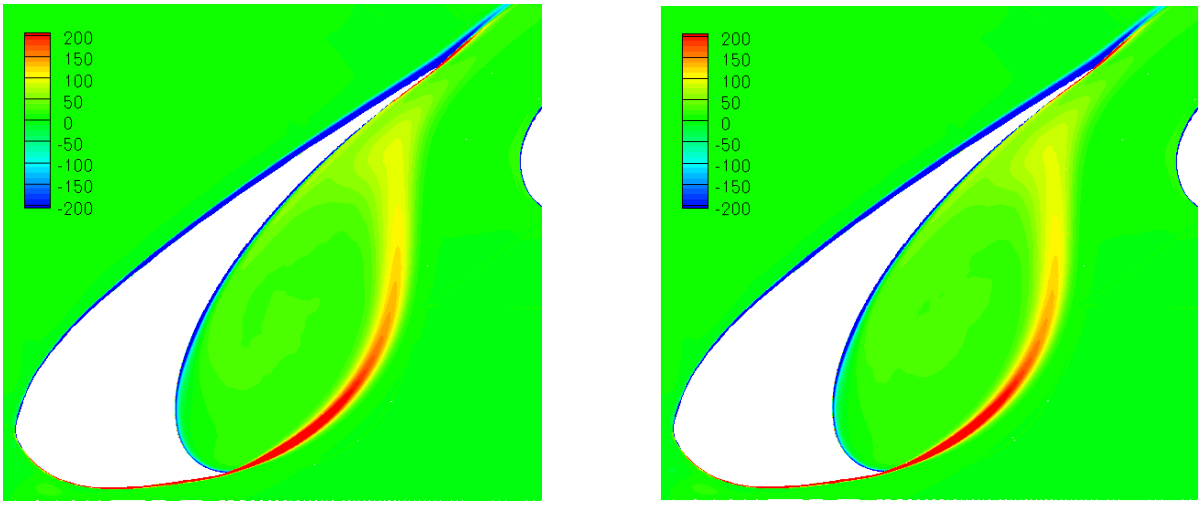

(a) $dt = 0.0016464$ (b) $dt = 0.0008232$

Figure 7. Spanwise vorticity, $\omega_z c/U_\infty$, around the slat averaged both temporally and in the spanwise direction.

The 2-D velocity magnitude from the finer time step calculation is shown in figure 9(a). Much of the unsteadiness in the slat region develops in the shear layer between the low velocity fluid in the recirculation region and the high velocity fluid that goes through the gap. Two normal cuts through the shear layer are identified in the figure which are used to quantitatively assess the calculation's ability to simulate the growth in the shear layer. Figure 9(b) compares the 2-D velocity profiles in these cuts to experimental Particle Image Velocimetry (PIV) results (shown as dashed lines) from Jenkins *et al.*[17] Although there are some discrepancies between the CFD and PIV, the spreading rate of the shear layer is similar. Furthermore, the overall level of agreement is similar to that observed for the coarser grid computation in reference 20. Both CFD predictions indicate that the peak velocities are lower than that observed in the PIV data, lending further credence to the hypothesis that the differences in the outer velocities are caused by the differences in the boundary conditions. The BART is a closed wind tunnel, whereas the simulations are performed in free air.

The trajectory of the shear layer is shown as the purple line in figure 9(a). The line defines the location of maximum shear as determined by the spanwise vorticity in figure 7. The termination of the trajectory is chosen to be the reattachment point as the location of maximum shear becomes ambiguous in this region. The distance along the shear layer trajectory is denoted by S, and S_{max} corresponds to where the trajectory terminates at the reattachment point. Along this line, the rms of the perturbation velocities and the 3D turbulent kinetic energy,

$$3D\ TKE\ =\ 1/2(< u'u' > + < v'v' > + < w'w' >)/U_\infty^2), \tag{1}$$

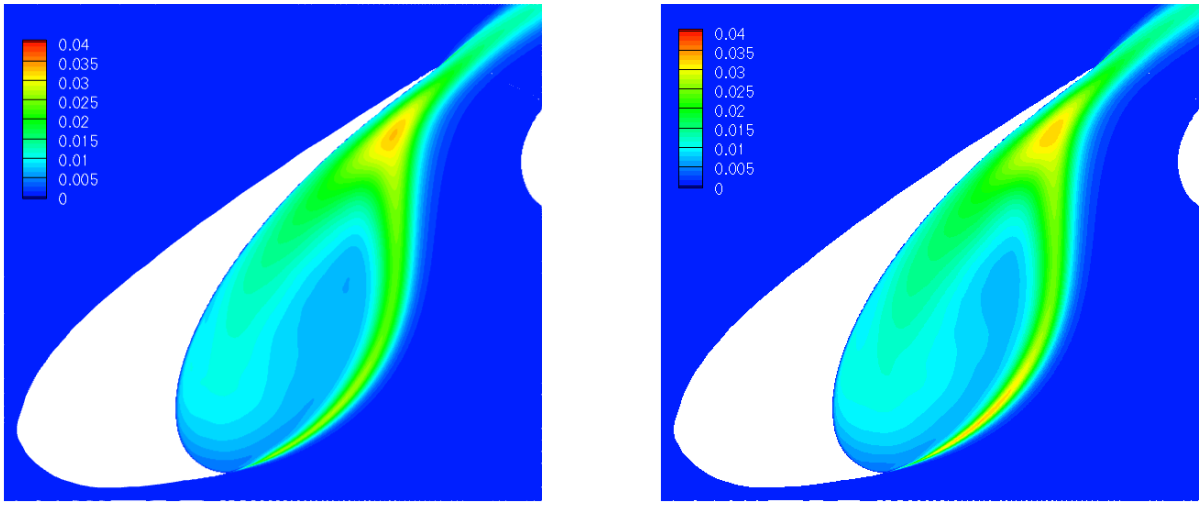

(a) $dt = 0.0016464$ (b) $dt = 0.0008232$

Figure 8. 2D Turbulent kinetic energy normalized by U_∞^2 around the slat averaged both temporally and in the spanwise direction.

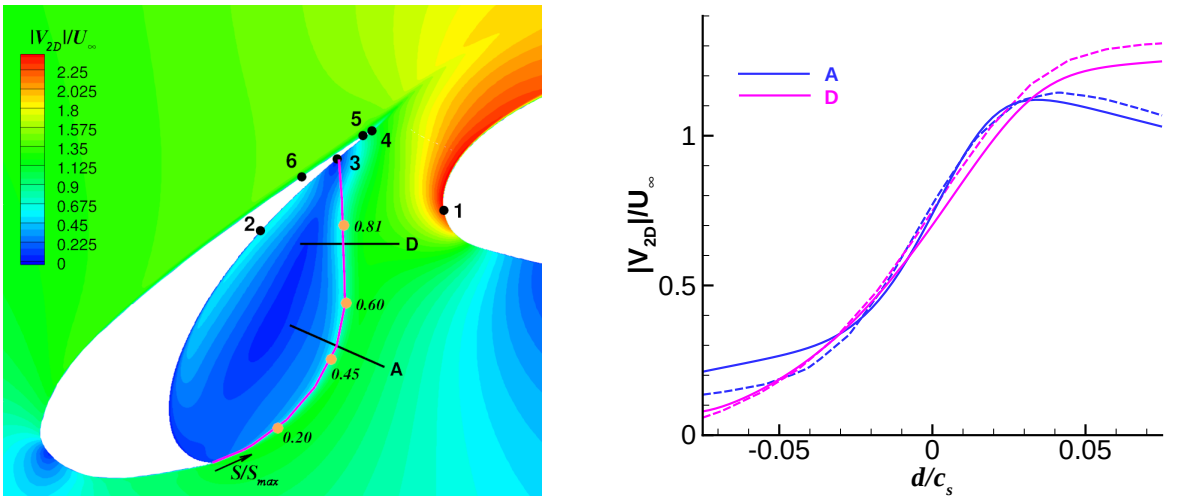

(a) $|V_{2D}|/U_\infty$ (b) 2-D Velocity Magnitude

Figure 9. (a) 2-D Velocity magnitude contours with lines indicating profiles through the shear layer. (b) 2-D Velocity magnitude profiles through the shear layer versus normal distance. Calculations used dt=0.0008232 and the PIV results (dashed lines) are from reference 17.

are presented in figure 10. Initially, the fluctuations in u' are strongest, but v' fluctuations quickly become dominant. The fluctuation levels are highest near the reattachment point, but they also have a local maximum around $S/S_{max} = 0.25$ along the shear layer trajectory. As can be seen in the instantaneous vorticity in figure 6(a), spanwise rollers initially grow rapidly and then begin to breakdown where the TKE has a local maximum. Finally, the vorticity is rapidly distorted as the structures approach the underside of the slat. First, the v' fluctuations are accentuated followed by intense w' fluctuations right near the reattachment point. This region of high distortion is associated with the highest fluctuation levels. All of the profile shapes in 10(a) are similar to those presented in reference 20. However, the plateau near the cusp is much more defined in the current simulation, and the peak levels near the reattachment point are around 20% higher. In the current simulations, the w' rise more rapidly as the shear layer approaches the underside of the slat. Beyond the obvious grid resolution explanation for the differences, the longer span in the current simulations may be allowing more three-dimensionality to develop.

The normalized 2-D turbulence intensity, $Tu_{2D} = 1/2\sqrt{< u'u' > + < v'v' >)}/U_\infty$ is compared with PIV results taken from the experiment in reference 17 but reported by Choudhari 20 who discovered that a small field-of-view (FOV) had to be used to resolve the rapid change in the turbulence intensity near the cusp. Unfortunately, the small FOV PIV

data is only available near the slat cusp. The agreement with the small FOV PIV is reasonable. Both show a rapid rise, then a plateau around $S/S_{max} = 0.09$, followed by another rapid rise. The large FOV PIV shows a peak around $S/S_{max} = 0.9$ which agrees with the simulation. In this region, the shear layer has spread sufficiently that the large FOV PIV has should have been able to resolve the gradients.

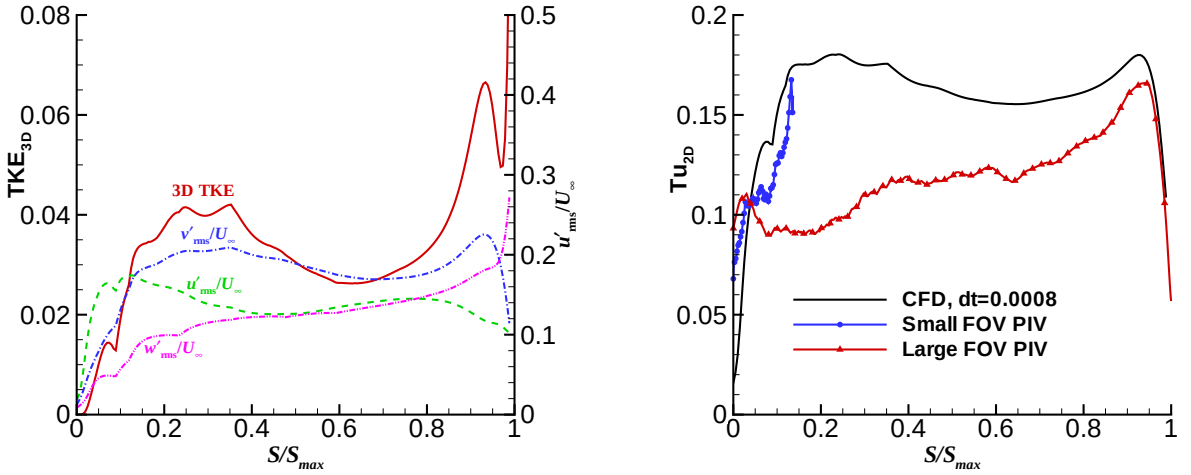

(a) 3D TKE and rms (b) Tu_{2D}

Figure 10. Profiles along the mixing layer trajectory shown in figure 9(a) (S denotes the distance from the cusp along the shear layer trajectory) (a) 3D TKE and velocity rms values (b) 2D Turbulence intensity from the calculation with dt=0.0008232 and PIV results from reference 17.

Having established an overall consistency with both previous computations and PIV data, we now expand the analysis to spectral information. Figure 11(a) presents the power spectral density of the v' fluctuations at 4 locations along the shear layer trajectory. The probe positions are shown as the orange circles in figure 9(a). The first 3 points correspond with those used in reference 20. The data was sampled at $4dt$ in the fine time-step calculation, and the analysis utilized 5 blocks of 4096 samples. Assuming spanwise homogeneity, the data was then averaged over the span. The spectra are plotted against a Strouhal number based on the chord of the slat, $St = fc_s/U_\infty$. Near the cusp where the shear layer is thinnest, the spectra exhibits a spectral peak at higher frequencies. These fluctuations occur away from the solid surfaces and edges; therefore, their contribution to the radiated noise is expected to be small. The progression of the spectral peak as the shear layer thickens is not obvious in v', but shows up clearly in all the other variables. Because the spectral features of ρ', p', u', and w' are similar, only the results for u' are presented. The spectral peak in the autospectrum of u' in figure 11(b) broadens and moves to lower frequencies as S increases. Close to the reattachment point, the peak is around $St = 2$. The current results show defined peaks for u', especially for the points further along the shear layer trajectory.

Spanwise correlation data for v' and u' at the 4 points are presented in figure 12(a) and (b), respectively. Because of the periodic boundary conditions, the correlation can only be calculated for spanwise separations up to half the length of the computational span. At all of the probe locations, the correlation drops relatively rapidly which is to be expected for a thin shear layer. However, The correlation drops more slowly than the results from the coarser grid computations in reference,[20] and only approaches zero around $\Delta z/c_s = 0.4$. Although the current computations have more grid points in the 2-D plane and should better resolve the dynamics in the shear layer, the spreading rate and fluctuation levels are quite similar between the computations. The probable reason for the discrepancy in the correlations in reference[20] is the extended spanwise dimension in the current simulations. When periodic boundary conditions are employed, the first and last points are identical and perfectly correlated. The spanwise extent must be sufficiently long to allow the flow to become completely decorrelated or the flow will be artificially affected by the periodicity. The current calculations indicate that a spanwise domain of 80% of the slat chord is needed for the velocity fluctuations in the shear layer, which is double what was used in the simulations of.[20] Nonetheless, the span of 2.26 c of the current simulations appears to be considerably more than required.

Although the correlation gives an overall indication of the similarity of the fluctuations at different spanwise locations, information about what is happening at select frequencies can easily be lost. Another way to look at the spanwise decorrelation function is through the coherence,

$$\gamma^2(f) = \frac{G_{v_1 v_2}(f)}{|G_{v_1 v_1}(f)||G_{v_2 v_2}(f)|} \tag{2}$$

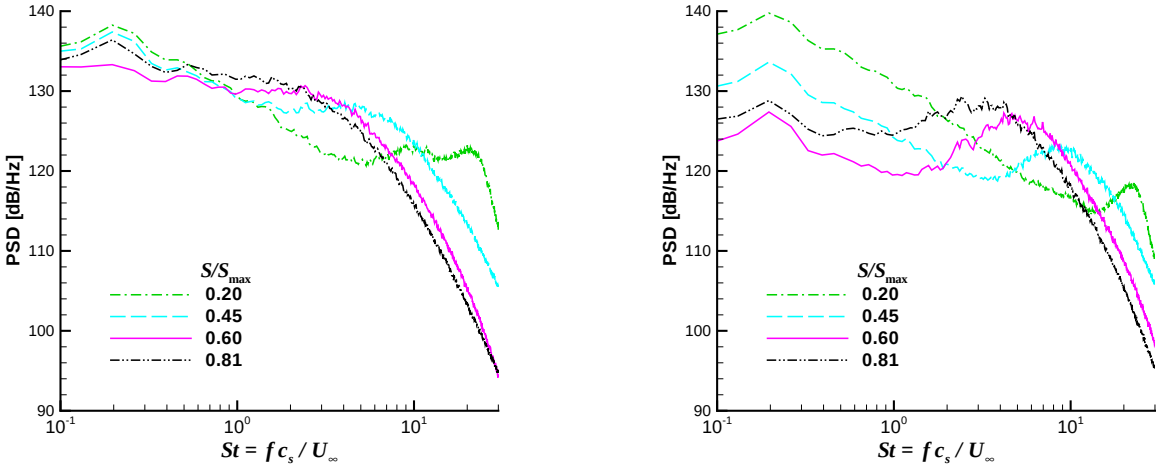

(a) Autospectra of v' (b) Autospectra of u'

Figure 11. Power spectral density of the perturbation velocities at several locations along the mixing layer trajectory shown in figure 9(a) (S denotes the distance from the cusp).

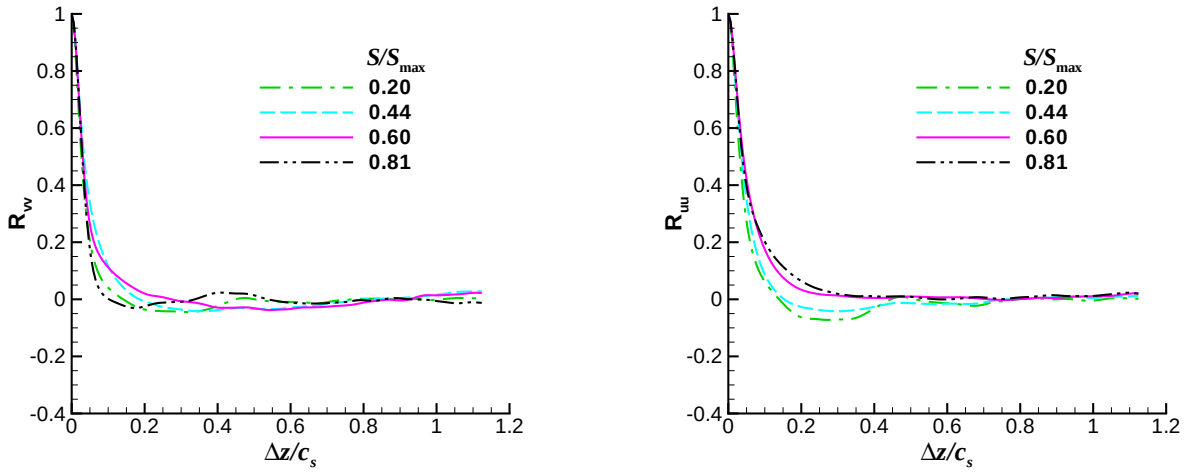

(b) Spanwise correlation of v' (b) Spanwise correlation of u'

Figure 12. Spanwise correlations at several locations along the mixing layer trajectory shown in figure 9(a) (S denotes the distance from the cusp).

where $Gv_1v_2(f)$ is the cross-spectral density function between the velocities at two spanwise locations. The coherence allows one to examine individual frequencies. Unfortunately, a coherence analysis produces a coherence versus spanwise separation distance for each frequency. The result for the $S/S_{max} = 0.81$ location is presented as a contour map in figure 13(a). Fortunately, the decay with spanwise distance at each frequency is reasonably approximated using a Gaussian function

$$\gamma^2(f) = \exp\left(-\left(\frac{\Delta z}{L_c(f)}\right)^2\right) \tag{3}$$

as shown in figure 13(b) for $St = 0.4$. The agreement at other frequencies is similar. Hence, the variation for each frequency can be reduced to a single coherence length scale, L_c. The parameter L_c is determined for each frequency using a least-squares fit of the data. Based on the Gaussian definition, the coherence length normalized by the slat chord for each of the points along the shear layer trajectory is presented in 14. To increase the number of samples available for averaging, the block size used in calculating the coherence is half that used in the autospectral analysis. The coherence length for v' decreases nearly monotonically with increasing frequency. However, the coherence length for u' is largest in the same frequency ranges where spectral peaks were observed in the autospectra. Furthermore, for the two points

closest to the reattachment region ($S/S_{max} = 0.6$ and 0.81, respectively), multiple, narrow band peaks are evident. The spacing between the peaks is not harmonic. However, they do correspond with peaks that are observed in some of the surface pressure spectra shown in figure 15(a) for the 6 points identified in figure 9(a). The peaks are strongest on the upper side of the slat (5 & 6) where the grid is too coarse to resolve boundary layer fluctuations, so the signal primarily represents acoustic radiation. Point 5 is close to the trailing edge, so some influence of evanescent waves generated by the scattering process is also likely to be present. Some hint of the peaks is also visible near the reattachment point (3) and near the trailing edge on the underside of the slat (4). The point inside the recirculation region (2) shows no indication of the peaks. Some of the peaks are evident at the point on the main element (1), whereas others are not. A spanwise coherence analysis has also been performed for the 6 points. A representative case is plotted in figure 15(b) that shows the level of agreement between the data and a Gaussian distribution for point 6 at $St = 0.4$. Figure 16(a) presents the coherence lengths as a function of Strouhal number for each of the points. The coherence length is relatively long (on the order of slat chord) for the two points dominated by acoustic radiation (1 and 6). They show similar levels except that the 2nd and 3rd peaks are considerably reduced on the main element. The results for points 1 and 6 have been removed in figure 16(b) to allow the range for the ordinate to concentrate on the behavior of the other points. Clearly, the peaks are discernible at all the locations except for the point in the recirculation zone. Although the coherence analysis has revealed some interesting features, it does not explain their cause. The spectral peaks seem associated most strongly with the points where there is primarily acoustic radiation, but whether this is because of the nature of the hydrodynamic fluctuations passing the trailing edge, the selective nature of the scattering mechanism, or some sort of geometric reinforcement is unclear. The absence of the features in the surface pressure spectra in the recirculation zone seem to preclude any sort of cavity resonance or global oscillation.

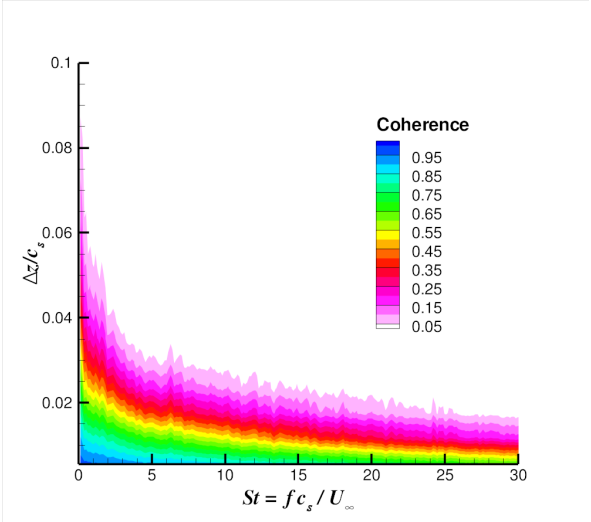

(a) Spanwise coherence

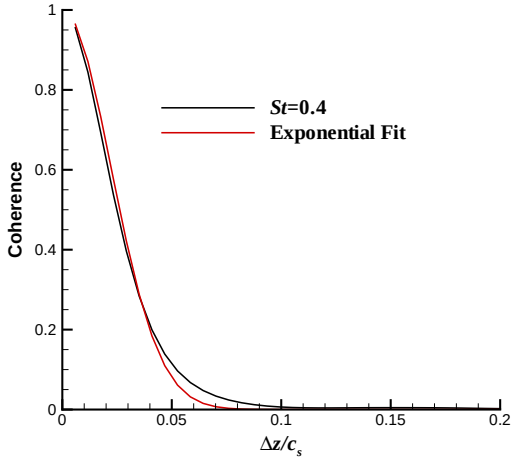

(a) Coherence for $St = 0.4$

Figure 13. Coherence of the perturbation vertical velocity at $S/S_{max} = 0.81$ (S denotes the distance from the cusp).

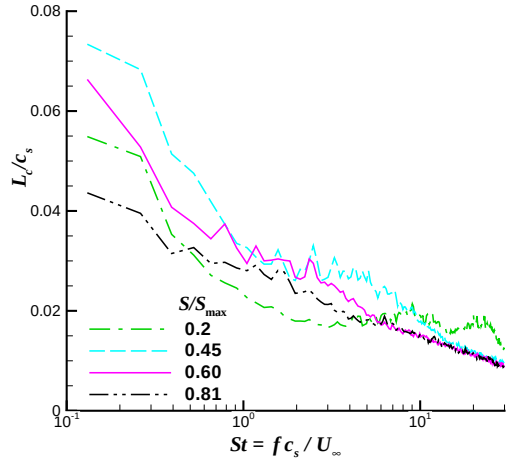

(b) Spanwise coherence length of v'

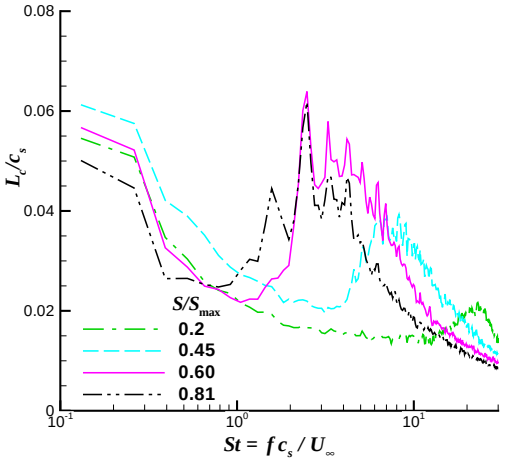

(b) Spanwise coherence length of u'

Figure 14. Coherence of the perturbation vertical velocity at several locations along the mixing layer trajectory shown in figure 9(a) (S denotes the distance from the cusp).

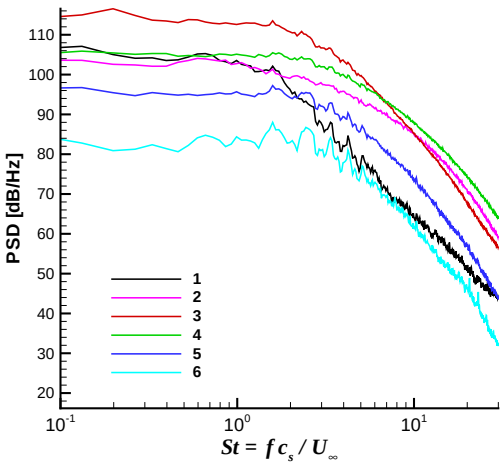

(a) Autospectra of p'

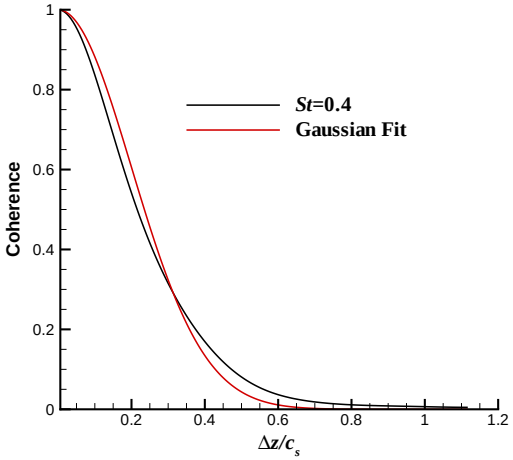

(b) Coherence at $St = 0.4$

Figure 15. Power spectral density and spanwise correlation of the perturbation pressure at several surface points identified in figure 9(a).

IV. Acoustic Calculations

The far-field noise was calculated using the Ffowcs Williams-Hawkings (FW-H) equation[27] solver described by Lockard.[28] Unsteady flow data from the CFD calculations was recorded on the surfaces shown in figure 17. In the figure the solid surface of the high-lift system is represented by the black line, and a porous surface is shown in red. The porous surface follows grid lines from the CFD computation. The discontinuities in the surface are a consequence of the topology of the blocks in the CFD grid. Other choices for the porous surface did not make a significant difference in the results. Although the plot is two-dimensional, the data was extracted over the full span of the CFD calculation. However, only half of the spanwise data (corresponding to 1.13 slat chords) was used in the FW-H calculations to avoid artificial interference effects caused by the periodic nature of the simulation. Given that the nearfield fluctuations have spanwise coherence length scales on the order of 0.1 slat chords, over 10 coherence lengths are still included. However, the propagating acoustics in the CFD was observed to have a coherence length of the order of a slat chord. Porous surfaces, which primarily see propagating acoustics, will be most affected by the long spanwise coherence length of the acoustics. However, the effects should be minimal for radiation in the plane of the airfoil where our primary interest lies,

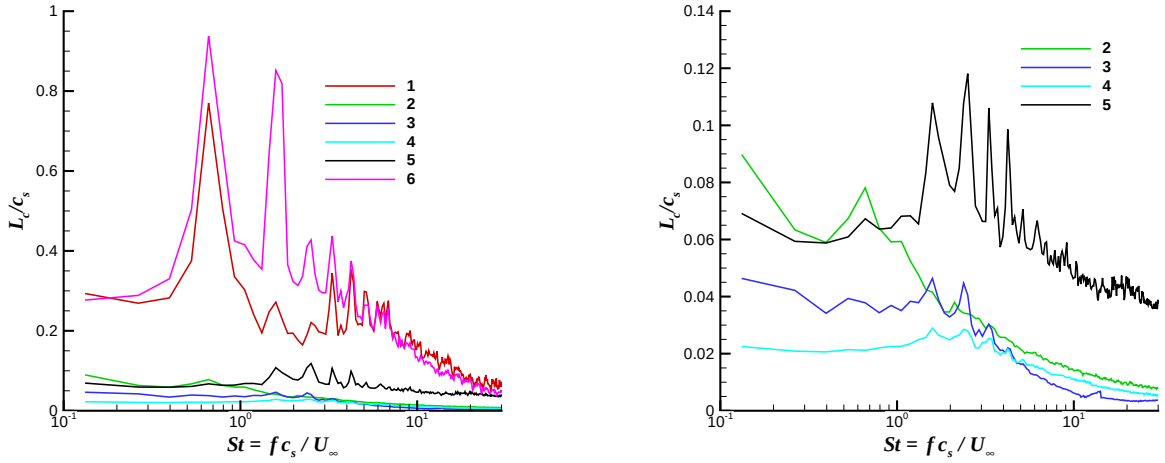

(a) Spanwise coherence length (b) Spanwise coherence length

Figure 16. Coherence of the perturbation pressure at the points identified in figure 9(a).

as we have not done anything to model real end effects in the CFD.

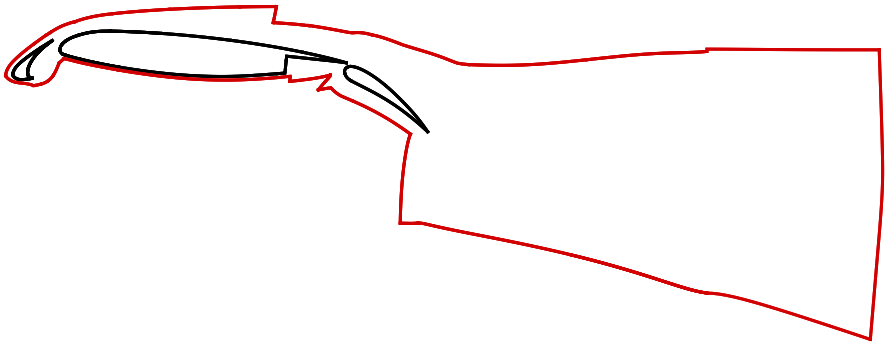

Figure 17. Surfaces used for FW-H calculations.

The overall sound pressure level (OASPL) calculated directly from the near-field CFD is presented in figure 18. The directivity shows a primary dipole source oriented at 135° with some interference effects caused by the geometry. The directivity is similar to that observed in the instantaneous pressure contours in figure 16(c) of reference 20 suggesting that the in-plane directivity pattern can be reasonably approximated using narrow domain simulations that allow for most of the spanwise decorrelation across the width of the domain. However, the absolute levels and details are likely to be different.

Figure 19(a) demonstrates that by a radius of 10 chords, the acoustics are effectively in the far-field as the FW-H prediction using solid surface data exhibits the expected $1/r$ dependence. The result using the porous surface is nearly identical. Unless otherwise noted, all of the observers are located in the mid-span of the data used as input to the FW-H. The power spectral density shown in figure 19(b) is for an observer at a radius of 10 chords and an angle of 290°, which is peak in the lower arc of the directivity. The agreement between all 4 spectra demonstrates the relative insensitivity of the noise to the time step and data surface. A Strouhal number based on the slat chord is used for the abscissa. The peak in the spectrum occurs around a Strouhal number of 2, which is in the range of 1-3 observed by other researchers[8] in nearfield measurements and also corresponds to the peak observed in the velocity fluctuations in the shear layer in figure 12(a). The spectra also exhibit multiple, narrow band peaks, some of which correspond with the peaks observed in the coherence analysis of the shear layer velocity fluctuations and surface pressure. Clearly, some connection between the two exists. The comparisons at other angles are in similar agreement although there is some discrepancy between solid and porous surface predictions for $St > 10$. Refraction effects are not explicitly accounted for in FW-H predictions, but any mean flow interaction that occurs within the FW-H surface is included. Therefore, the porous surface predictions include some nonuniform flow effects (as determined up to the FW-H surface by the underlying CFD calculation), but

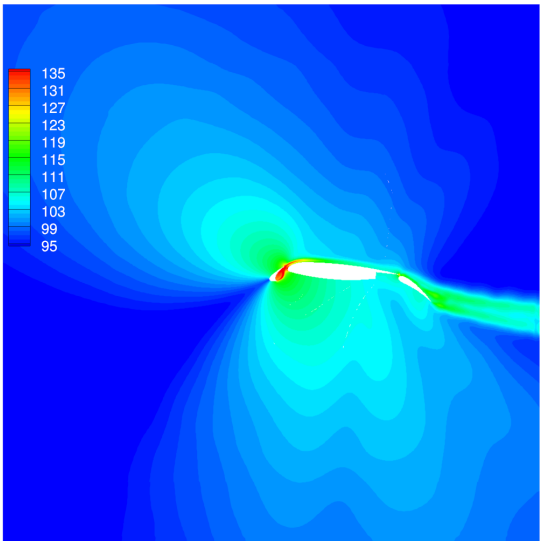

Figure 18. OASPL calculated directly from the CFD with $dt = 0.0008232$.

the predictions using the solid surface data do not include any mean flow effects. However, the slat spectra shows very little energy beyond $St = 10$, so the overall importance of refraction appears to be minimal.

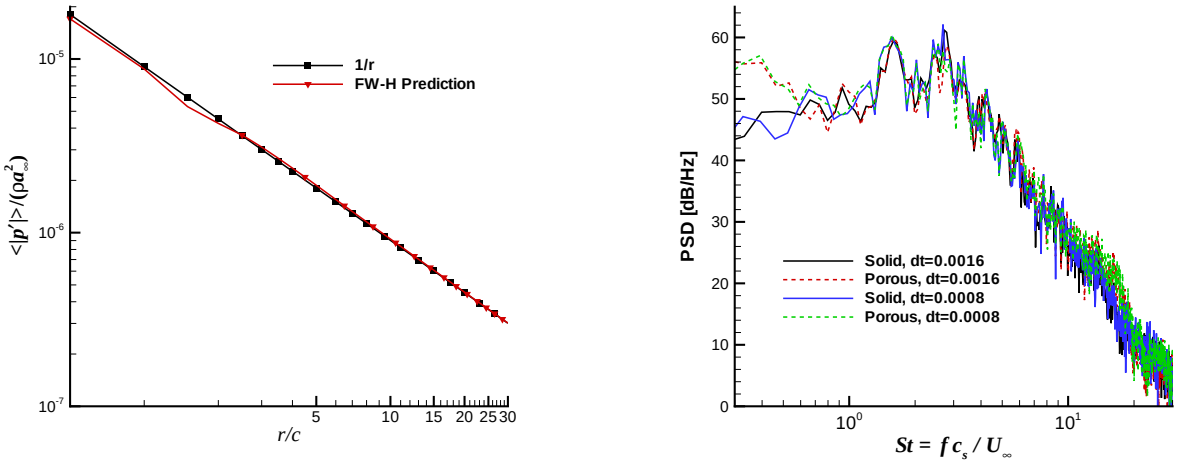

(a) Radial variation

(b) Spectra at $r = 10c$

Figure 19. Spectra and radial variation of the acoustics signal along $290°$.

The near-field directivity in figure 18(a) can be compared with the far-field directivity computed using the FW-H equation. The directivity for observer locations within the mid-span plane and a radius of 10 chords from the airfoil is given in figure 20(a). Results for both the solid and porous FW-H surfaces as well as both time steps are included in the figure. For the larger time step, data was collected over 30,000 time steps. The data were divided into 6 segments with 50% overlap and run through the FW-H code. The results in the figure represent the average over all the segments. For the smaller time step, data were collected over 52,000 time steps giving 5 segments with 50% overlap. The directivity results show only a slight dependence on the choice of the data surface. The porous surface calculation includes refraction effects inside the surface, so slight differences should be expected. Also, the figure shows that the time step has not had a significant impact on the radiated noise in agreement with the Cp'_{rms} analysis on the airfoil surface.

The narrow band directivity across selected bands of Strouhal number is presented in figure 20(b). The solid FW-H surface was used to produce the results using the small time step data. The Strouhal numbers listed give the centers of the bands. At the lowest frequency, the radiation is primarily in the downstream direction. The pattern is similar to that of the overall directivity for $St = 1.25$ and 2.75. At $St = 5.75$, most of the radiation is upstream and directly below the

airfoil. Above $st = 5.75$, there is not enough energy in the signal to effect the overall directivity.

The directivity in the $z - y$ plane is presented in figure 21. Although the CFD simulation did not include any end effects and employed a relatively narrow span, the computed directivity from the FW-H calculation using the solid surface data should give some general indication of the radiation in the spanwise direction. As the figure shows, the directivity is of dipole nature. For a much longer span, one would expect the top and bottom lobes to be flatter as a result of the decorrelated contributions from all the spanwise stations.

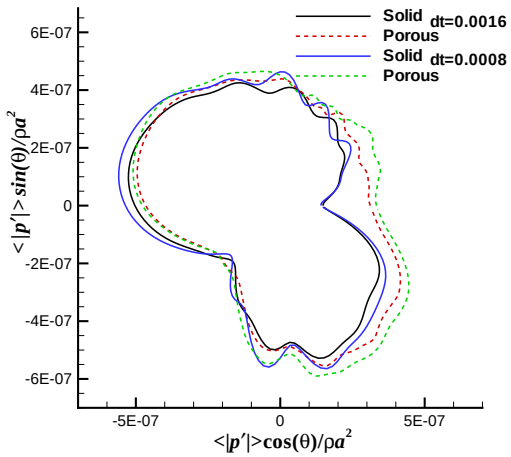

(a) Overall directivity

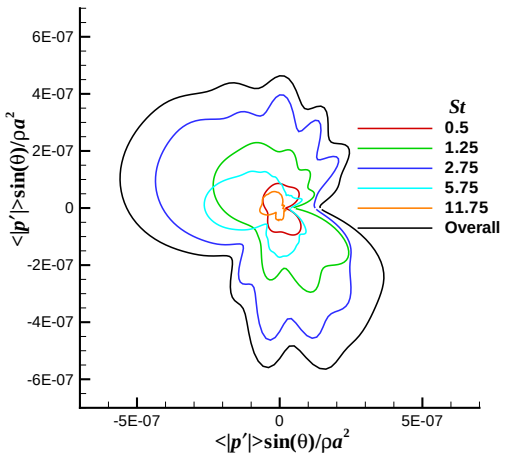

(a) Directivity using solid surface

Figure 20. Acoustic directivity results for observers located 10 chords from the airfoil.

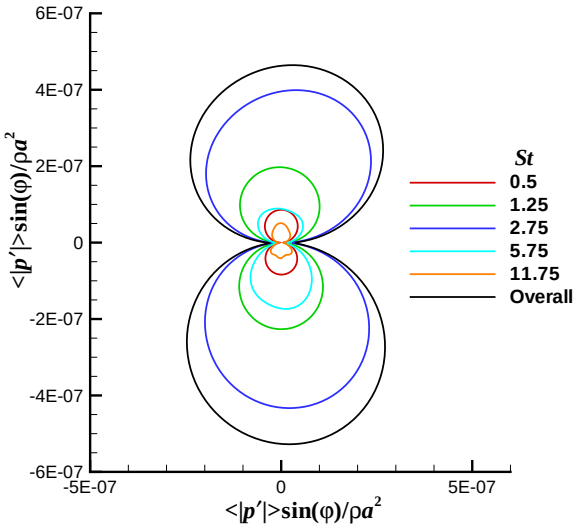

Figure 21. Acoustic directivity results for observers located 10 chords from the airfoil in the $z - y$ plane.

One of the reasons for using a span of 2.26 slat chords in the current computations was to allow for some three-dimensionality in the acoustic radiation. Figures 22 and 23 show the instantaneous perturbation density fluctuations 0.6 and 3 chords below the airfoil, respectively. The aspect ration in the figure has been altered to allow the strip in the vicinity of the airfoil to be examined in more detail. The airfoil resides between $x = 0$ and 10 in the coordinate system of the figure. The entire computational domain in the spanwise direction (33% of the chord) is included in the vertical direction. Although the solution at $y/c = -0.6$ is comprised of many spanwise modes, the periodic boundary conditions employed in the simulations are restricting the number of modes in the results at $y/c = -3.0$. Nonetheless, the acoustic radiation is still exhibiting more than purely two-dimensional behavior as several modes are apparent.

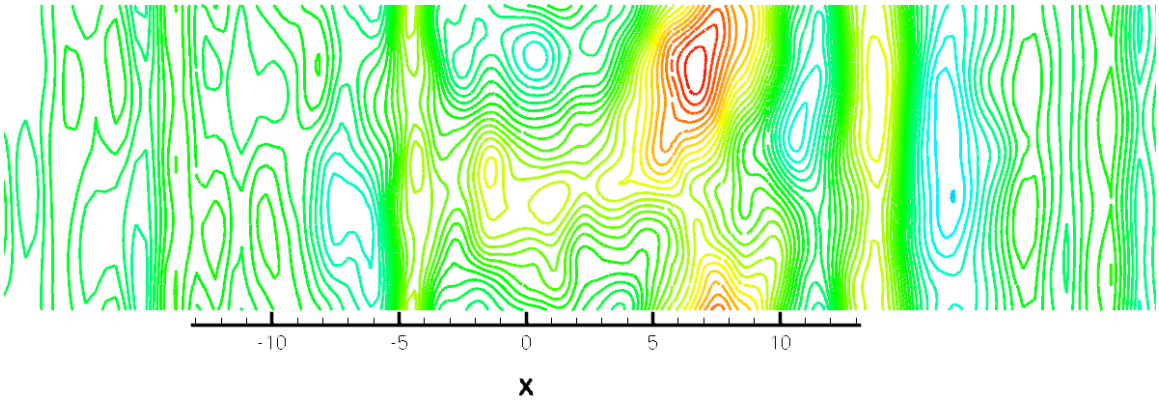

Figure 22. Perturbation density fluctuations 0.6 chords below the airfoil.

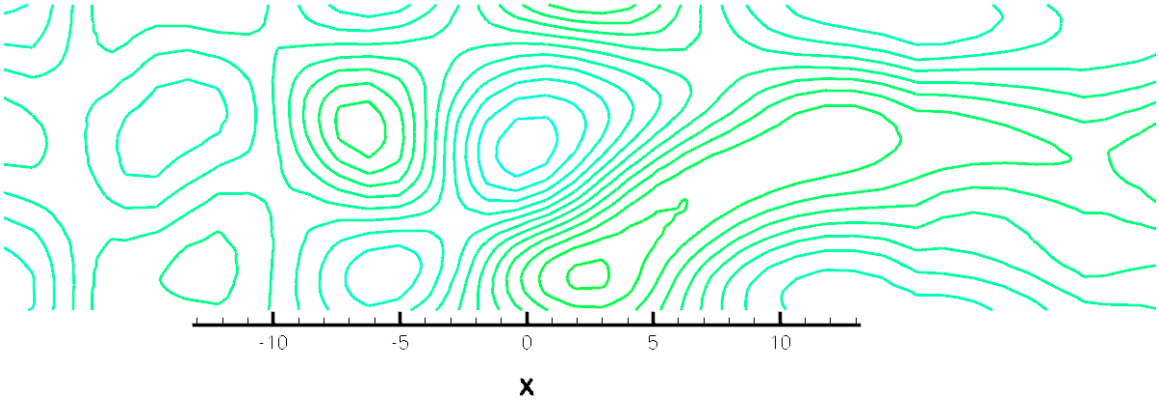

Figure 23. Perturbation density fluctuations 3 chords below the airfoil.

V. Conclusions

An extensive dataset has been collected that is being used to examine the character of slat noise sources in a generic high-lift configuration. The current 3D simulations have been shown to be in reasonable agreement with the experimentally observed unsteady flow behavior. Although the spanwise domain would still be considered small experimentally, the current spanwise extent of nearly 226% of the slat chord (i.e., 15% of the model span) is a considerable improvement over previous simulations. The complete spanwise decorrelation in the nearfield fluctuations has been captured allowing far-field noise predictions without invoking extensive assumptions about the spanwise variation of the flow. The results indicate that the major features of the slat cove flow can be adequately captured using a span of 80% of the slat chord and periodic boundary conditions, although the radiated acoustics is much more correlated with a coherence length of around a slat chord. Enhanced coherence was found at certain discrete frequencies in the near field data that correspond to peaks in the spectrum of the acoustics. The investigation into the mechanism behind the connection is ongoing. The acoustic spectra display a broad peak around a Strouhal number based on the slat chord of 2 to 3, and this corresponds with nearfield spectral peaks and enhanced coherence in most of the primitive variables. However, the nearfield v' fluctuations do not exhibit this behavior. The observed directivity pattern in the plane of the airfoil is similar to that found by previous researchers and would be reasonably approximated by a dipole normal to the trailing edge of the slat. The directivity in spanwise and vertical directions is also of dipole nature. Further analysis of the large dataset is ongoing, and future work includes the investigation of a more realistic configuration with sweep by imposing a spanwise flow.

Acknowledgments

The authors gratefully acknowledge the assistance of Mr. M.R. Wiese from the Analytical Services and Materials, Inc., who generated the computational grid used during the present study.

References

[1]Hayes, J. A., Horne, W. C., Soderman, P. T., and Bent, P. H., "Airframe Noise Characteristics of a 4.7% Scale DC-10 Model," 1997.

[2]Storms, B. L., Ross, J. C., Horne, W., Hayes, J., Dougherty, R. P., Underbrink, J. R., Scharpf, D. F., and Moriarty, P. J., "An Aeroacoustic Study of an Unswept Wing with a Three-Dimensional High Lift System," NASA TM 112222, February 1998.

[3]Dobrzynski, W., Nagakura, K., Gehlhar, B., and Buschbaum, A., "Airframe Noise Studies on Wings with Deployed High-Lift Devices," AIAA Paper 1998-2337, 1998.

[4]Storms, B. L., Hayes, J. A., Moriarty, P. J., and Ross, J. C., "Aeroacoustic Measurements of Slat Noise on a Three-Dimensional High-Lift System," AIAA Paper 1999-1957, 1999.

[5]Choudhari, M. M., Lockard, D. P., Macaraeg, M. G., Singer, B. A., Streett, C. L., Neubert, G. R., Stoker, R. W., Underbrink, J. R., Berkman, M. E., Khorrami, M. R., and Sadowski, S. S., "Aeroacoustic Experiments in the Langley Low-Turbulence Pressure Tunnel," NASA TM-211432, February 2002.

[6]Mendoza, F. and Brooks, T., "Aeroacoustic Measurements of a Wing/Slat Model," AIAA Paper 2002-2604, 2002.

[7]Chow, L. C., Mau, K., and Remy, H., "Landing Gears and High Lift Devices Airframe Noise Research," AIAA Paper 2002-2408, 2002.

[8]Dobrzynski, W. and Pott-Pollenske, M., "Slat Noise Source Studies for Farfield Noise Prediction," AIAA Paper 2001-02158, 2001.

[9]Guo, Y., Yamamoto, K., and Stoker, R., "Component Based Empirical Model for High-Lift System Noise Prediction," *Journal of Aircraft*, Vol. 40, No. 5, 2003, pp. 914–922.

[10]Guo, Y. and Joshi, M., "Noise Characteristics of Aircraft High-Lift Systems," *AIAA Journal*, Vol. 41, No. 7, 2003, pp. 1247–1256.

[11]Khorrami, M. D., Berkman, M. E., and Choudhari, M., "Unsteady flow compuations of a slat with a blunt trailing edge," *AIAA Journal*, Vol. 38, No. 7, 2000, pp. 1558–1564.

[12]Singer, B. A., Lockard, D. P., and Brentner, K. S., "Computational Aeroacoustic Analysis of Slat Trailing-Edge Flow," *AIAA Journal*, Vol. 38, No. 9, 2000, pp. 1558–1564.

[13]Khorrami, M. R., Singer, B. A., and Berkman, M. E., "Time-accurate Simulations and Acoustic Analysis of Slat Free Shear Layer," *AIAA Journal*, Vol. 40, No. 7, 2002, pp. 1284–1291.

[14]Khorrami, M. R., Singer, B. A., and Lockard, D. P., "Time-accurate Simulations and Acoustic Analysis of Slat Free Shear Layer: Part II," AIAA Paper 2002-2579, 2002.

[15]Choudhari, M., Khorrami, M. R., Lockard, D. P., Atkins, H. L., and Lilley, G. M., "Slat Cove Noise Modeling: A Posteriori Analysis of Unsteady RANS Simulations," AIAA Paper 2002-2468, 2002.

[16]Khorrami, M. R., Choudhari, M. M., and Jenkins, L. M., "Characterization of Unsteady Flow Structures Near Leading-Edge Slat: Part II. 2-D Computations," AIAA Paper 2004-2802, Presented at the AIAA/CEAS Aeroacoustics Conference, Manchester, UK, May 10–12, 2004.

[17]Jenkins, L. M., Khorrami, M. R., and Choudhari, M. M., "Characterization of Unsteady Flow Structures Near Leading-Edge Slat: Part I. PIV Measurements," AIAA Paper 2004-2801, Presented at the AIAA/CEAS Aeroacoustics Conference, Manchester, UK, May 10–12, 2004.

[18]Rakhshani, B. and Filippone, A., "Three-Dimensional CFD Analysis of Slat Noise," AIAA Paper 2008-0015, 2008.

[19]Imamura, T., Enomoto, S., Yokokawa, Y., and Yamamoto, K., "Three-Dimensional Unsteady Flow Computations Around a Conventional Slat of High-Lift Devices," *AIAA Journal*, Vol. 46, No. 5, 2008, pp. 1045–1053.

[20]Choudhari, M. M. and Khorrami, M. R., "Effect of Three-Dimensional Shear-Layer Structures on Slat Cove Unsteadiness," *AIAA Journal*, Vol. 45, No. 9, 2007, pp. 2174–2186.

[21]Klausmeyer, S. M. and Lin, J., "Comparative Results from a CFD Challenge Over a 2D Three-Element High-Lift Airfoil," NASA TM 112858, May 1997.

[22]Rumsey, C. L., Biedron, R. T., and Thomas, J. L., "CFL3D: Its History and Some Recent Applications," NASA TM 112861, May 1997, presented at the Godonov's Method for Gas Dynamics Symposium, Ann Arbor, MI.

[23]Krist, S. L., Biedron, R. T., and Rumsey, C. L., "CFL3D User's Manual (Version 5)," NASA TM 208444, NASA Langley Research Center: Computational Aerosciences Branch, 1997.

[24]Menter, F. R., "Zonal Two-equation k-w Turbulence Models for Aerodynamic Flows," AIAA Paper 1993-2906, 1993.

[25]Menter, F. R., "Two-equation Eddy-viscosity Turbulence Models for Engineering Applications," *AIAA Journal*, Vol. 32, No. 8, 1994, pp. 1598–1605.

[26]Khorrami, M. R., Lockard, D. P., Choudhari, M. M., Jenkins, L. N., Neuhart, D. H., and McGinley, C. B., "Simulations Of Bluff Body Flow Interaction For Noise Source Modeling," AIAA Paper 2006-3203 Presented at the 36th AIAA Fluid Dynamics Conference and Exhibit, San Francisco, CA, United States, June 5-8, 2006.

[27]Ffowcs Williams, J. E. and Hawkings, D. L., "Sound generation by turbulence and surfaces in arbitrary motion," *Philosophical Transactions of the Royal Society of London A*, Vol. 342, 1969, pp. 264–321.

[28]Lockard, D. P., "A Comparison of Ffowcs Williams-Hawkings Solvers for Airframe Noise Applications," AIAA Paper 2002-2580, 8th AIAA/CEAS Aeroacoustics Conference, Breckenridge, CO, June 17–19, 2002.